Experimental characterization and modelling of UO_2 grain boundary cracking at high temperatures and high strain rates

Salvo Maxime, Jérôme Sercombe, Thomas Helfer, Philippe Sornay, Thierry Désoyer

Experimental characterization and modeling of UO_2 grain boundary cracking at high temperatures and high strain rates

Maxime Salvo[a], Jérôme Sercombe[a], Thomas Helfer[a], Philippe Sornay[b] and Thierry Désoyer[c]

[a] CEA, DEN, DEC/SESC/LSC, F-13108 Saint-Paul-lez-Durance, France,
[b] CEA, DEN, DEC/SPUA/LCU, F-13108 Saint-Paul-lez-Durance,
[c] CNRS, LMA, 13402 Marseille Cedex 20, France.

Abstract

In this paper, the behavior of a dense UO_2 (porosity less than 2%) was studied experimentally on a range of temperatures (1100°C - 1700°C) and strain rates ($10^{-4} - 10^{-1}$/s) representative of RIA loading conditions. The yield stress was found to increase with strain rate and to decrease with temperature. Macroscopic cracking of the samples was apparent after the tests at 1100°C. Scanning Electron Microscopy (SEM) image analyses revealed a pronounced grain boundary cracking in the core of the samples tested at 10^{-1}/s and at 1550-1700°C. A hyperbolic sine model for the viscoplastic strain rate with a clear dependency on porosity was first developed. It was completed by a Drucker-Prager yield criterion with associated plastic flow to account for the porosity increase induced by GB cracking. Finite Elements simulations of the compression tests on the dense UO_2 were then successfully compared to the stress-strain curves, post-test diameter profiles and porosities at the pellets' center, periphery and top extremity. The response of the GB cracking model was then studied in biaxial compression, this condition being closer to that of the pellet during a RIA power transient.

Introduction

During simulated Reactivity Initiated Accidents (RIA) in experimental reactors (CABRI [1], NSRR [2], BIGR [3]), the fuel pellets experience high compressive and tensile stresses, in all or part of their volume [4]. In consequence, radial and axial cracks develop at the pellets' periphery [5] and fuel fragmentation characterized by grain boundary cracking may also take place [1,6]. The latter tends to increase significantly fission gas release during a simulated RIA transient and must therefore be considered in fuel performance codes. Fuel fragmentation is usually attributed to overpressure in

the gas bubbles situated at the grains interface [7] and treated in fission gas models at the grain scale [8–10].

Grain boundary cracking is however not limited to RIA transients but can also be observed at relatively low strain levels $\sim 1-2\%$ after strain-driven compression tests, compression creep tests or bending creep experiments on fresh fuel [11–16]. Hence gas overpressure might not be the only important parameter for grain boundary cracking. The possible connexion with RIA simulated tests is the stress level and temperature sustained by the fuel pellets. In strain-driven compression tests, a minimum stress ($\sim$60 MPa) and temperature ($\sim$1200°C) are required for the fuel to show signs of grain boundary cracking [11]. It is worth emphasizing that grain boundary cracking can initiate under macroscopic compressive stresses. In this respect, micromechanical numerical simulations of UO_2 show that strain incompatibilities between the grains can lead locally to tensile stresses [17, 18] at the origin of microcracking. In strain-driven compression tests, it is well known that the yield stress increases with the strain rate [19, 20]. This may explain why high strain rates trigger grain boundary cracking [14].

Porosity in uranium dioxide is also known to be a parameter of primary importance with respect to the yield stress and fracture strength of the material [21, 22]. The localization of pores, i.e., whether predominantly in the grains (intragranular) or at the grain boundaries (intergranular), but also the size and shape of pores (round or angular), have a strong impact on the material properties and the potential grain boundary cracking during mechanical tests [23–25]. In a recent experimental study, it was shown that very dense fuels (relative density $> 98\%$) with a small amount of intergranular pores tend to be more prone to grain boundary cracking during compressive creep experiments [16] (grain size being identical).

In this paper, an experimental work aiming at defining the temperature - stress conditions leading to grain boundary cracking in UO_2 is first presented. Strain rate controled compression tests are performed on a dense UO_2 at four strain rates ($10^{-4} - 10^{-3} - 10^{-2} - 10^{-1}$/s) and temperatures ($1100 - 1350 - 1550 - 1700$°C) representative of RIA conditions. In a second part, a creep - grain boundary cracking macroscopic constitutive model for UO_2 is proposed based on an extension of a previously published creep model [26]. Results from Finite Element (FE) simulations of uniaxial and biaxial compression tests are then detailed to illustrate the 3D stress - temperature domain where grain boundary cracking can be expected.

1 Experiments

1.1 Characterization of test samples

The samples used in this study are laboratory fabricated uranium dioxide cylindrical pellets of approximately 8.2 mm in diameter (d_0) and 15 mm in height (h_0). Commercial UO_2 powders were mixed and cold-grinded prior to sintering to obtain a material with particles of uniform size, ~ 1 μm in diameter. The powder was then cold-pressed at 600 MPa and sintered during 4 hours at 1700°C in a reducing atmosphere (95%Ar-5%H_2). The resulting oxygen/uranium ratio of the material was close to 2 (stoichiometry). Measures of the total porosity (f), of the open and closed porosities were obtained by weighing the dry sample (dry weight), the sample during immersion in alcohol (from which the volume of the sample is deduced) and the sample full of alcohol ("wet" weight). The open porosity is deduced from the difference between the "wet" and dry weight of the sample. The relative density ρ/ρ_{th} is estimated from the dry weight and from the sample volume (assuming a theoretical density $\rho_{th} = 10.96$ g/cm^3). The total porosity relates as follows to the relative density: $f = (1 - \rho/\rho_{th})$. The closed porosity is then deduced from the total and open porosities. The relative density of the material d reached 98.1% on average with a standard deviation of 0.2%. The porosity f consisted almost entirely of closed pores (i.e., non connected cavities): 1.9% with a standard deviation of 0.2%.

Some samples were then sawed, the surfaces coated with an epoxy resin and polished prior to their observations by Scanning Electron Microscopy (SEM), see Figure 1. From the SEM images, the average grain size was manually found close to 14 μm (calculated as the average of the grains situated on 4 intersecting lines). The commercial software ProAnalysis® was used to estimate the pore size distribution from the images.

The surface porosity appeared fairly uniform in the samples. On average, it reached 2.3% with a standard deviation of 0.6%. Half of the pore volume was formed of pores with a diameter less than 3 μm. These fine pores were mostly located in the grains. The greater pores (> 3 μm) were in majority located at the grain boundaries. The maximum pore size was close to the average grain size (~ 15 μm).

1.2 Test matrix and procedure

The testing equipment is shown schematically in Figure 2. Mechanical tests on the fuel pellets have been performed with an Instron 1185 compression test machine with a maximum load capacity of 50 kN. The compression machine

is equipped with an oven able to heat the fuel to a maximum temperature of 1800°C. The gas composition in the oven is controlled (95% Ar, 5% H_2) in order to prevent any stoichiometry change during the tests.

Strain-rate driven tests have been carried out on the pellet samples. In the tests, the displacement rate of the cross head is kept constant until a final discharge. The tests were performed at four prescribed temperatures: 1100, 1350, 1550 and 1700°C. At each temperature, four samples were tested with a displacement rate increased by decades from a minimum of 0.1 mm/min until a maximum of 100 mm/min (leading corresponding strain rates between 10^{-4}/s and 10^{-1}/s). Some of the tests were doubled or tripled to check the reproductibility.

The testing procedure reads as follows. First, the sample is placed between the two tungsten end-plates, see Figure 2, right. A small load not exceeding 250 N (5 MPa) is then applied. The gas composition in the oven is checked. The temperature is then increased manually until it reaches 200°C. This manual step is followed by a ramp at 20 °C/min until the prescribed temperature. These conditions are maintained 2 hours in order to guarantee a uniform temperature in the sample. The strain rate-driven loading sequence is then applied.

During the test, the speed of the cross-head is regulated and the contraction-elongation of the pellet is measured continuously by two extensometers in contact with the lower and upper Tungsten plates. From these measurements, the true strain ε_{zz} of the pellet is calculated according to Equation 1 where the deformed height of the pellet is considered ($h = h_0 + \Delta h$ with Δh the variation in height). In a first approximation, the axial stress σ_{zz} is estimated from the force F measured by the load cell and from the non-deformed diameter d_0 of the pellet, see Equation 2.

$$\varepsilon_{zz} = \ln\left(\frac{h}{h_0}\right) \tag{1}$$

$$\sigma_{zz} = -\frac{4F}{\pi d_0^2} \tag{2}$$

2 Test results

2.1 Stress-Strain curves

The stress-strain curves obtained in all the tests are presented in Figure 3 (grouped by strain rate) and Figure 4 (grouped by temperature). The general

tendency is an increasing stress with the strain rate and a decreasing stress with temperature. Apparent strain-hardening can also be observed in most of the tests at 1550°C and 1700°C (Figure 4).

At 1350°C, the behaviour appears more complex with a stress peak at 1% strain followed by a decrease of the stress till ∼1.5-2.5% strain and then a pronounced strain-hardening. The magnitude of the stress peak increases with the strain rate. A similar behavior was obtained by Guérin [20] and Sauter and Leclercq [27] in their strain-rate controlled compressive tests. The first author attributed the stress peak to structural effects (stress and strain inhomogeneity in the pellet due to friction at pellet ends) and showed that its magnitude depended on the diameter/height ratio of the pellet. The second authors introduced a dislocation based viscoplastic model to account for this phenomenon (referenced as yield point in the paper and attributed to a cascade of dislocations) at material level.

The stress-strain curves at 1100°C differ from the ones obtained at the other temperatures. A stress peak is also apparent but it is in most cases not followed by a strain hardening phase. At strain rates greater or equal to 10^{-3}/s, the behavior of the material after the stress peak is characterized by a softening (negative stress-strain slope) which increases with the strain rate. Significant strains are nevertheless reached in the tests (5-10%).

2.2 Macroscopic evolution

The shape of the samples after the tests are shown in Figure 5. Only the samples tested at the smallest temperature (1100°C) or at the highest strain rate (10^{-1}/s) exhibited significant cracking. The cracks are mostly situated at the pellet center and orientated in the loading direction (axial). The test at 1100°C and 10^{-1}/s led to the complete failure of the sample. The remains of the pellet are characterized by the formation of several axially orientated micro-columns that obviously failed by shear cracking (oblique cracks with respect to the direction of loading). This failure mechanism is typical of granular materials tested in compression [28].

To estimate volume variations during the tests, the residual diameter of the pellets $d(z)$ was systematically measured at ten regularly spaced points along three generatrices. The hoop strain axial profile $\varepsilon_{\theta\theta}(z)$ was then estimated according to :

$$\varepsilon_{\theta\theta}(z) = \ln\left(\frac{d(z)}{d_0}\right) \tag{3}$$

A fit of the diameter axial profile with a quadratic function was then used

to estimate the post-test average diameter of the pellet d_{av} and the volume variation $\Delta V/V$. In Figure 6, the average residual hoop strains calculated with Equation 3 from the average diameters, are plotted in function of the residual axial strains. The tests at 1100°C are not included in the linear regression of Figure 6 since the diameter profiles were strongly asymmetric due to the pronounced cracking of the pellets. The slope of the hoop versus axial strain regression curve is very close to -0.5 (-0.495), indicating that no significant volume variation took place during the tests. This result differs from the 1-2% volume variation obtained in a previous study on a UO_2 with 4% initial porosity [26]. The 2% difference in porosity with respect to the material studied in this work is mainly concentrated at the grain boundaries.

The samples' volume variation during the tests was also systematically estimated from hydrostatic density measurements. Figure 7 (top graph) summarizes the evolution with temperature and strain rate. Consistent with the diameter measurements, the volume variation of the samples is in general small ($< 0.3\%$) except at 1100°C and at the highest strain rate (10^{-1}/s). Interestingly, it changes sign with temperature. While it is positive at 1100 and 1350°C, it is negative at 1550 and 1700°C (with the notable exception of the test at 10^{-1}/s). This indicates that the samples were damaged at the smallest temperatures while they densified at the highest temperatures.

The evolution of the open porosity (representative of the crack density) from density measurements is given in Figure 7 (central graph). A small increase of the open porosity is obtained at 1350, 1550 and 1700°C ($\leq 0.2\%$) except at the highest strain rate where it reaches 0.5%. On the contrary, at 1100°C, the open porosity is always greater than 0.5% which is consistent with the pronounced damage of the samples. The evolution of the closed porosity of the samples with temperature and strain rate is given in Figure 7 (bottom graph). The small densification observed in the top graph of Figure 7 at 1550 and 1700°C leads to a $0.2-0.5\%$ decrease of the closed porosity. At 1100°C and 1350°C the variation in closed porosity remains small ($< 0.3\%$) but is positive.

In summary, there is a small decrease of the closed porosity at the highest temperatures (1550 and 1700°C) which is counterbalanced by a small increase of the open porosity. The resultant volume variation is close to null. There is one exception to this trend which concerns the sample tested at 1700°C and 10^{-1}/s. The important increase of open porosity is consistent with the observed post-test cracks in the pellet (Figure 5). At 1350°C, both the open and closed porosity increase moderately leading to a small volume variation ($< 0.5\%$). At 1100°C, the open porosity increases sharply in consequence of the pronounced cracking of the samples.

2.3 Microstructure evolution

SEM image analyses were performed on all the tested samples to study the evolution of the microstructure. The technique is described in Section 1.1. The samples were sawn along the (r, z) plane. Three different locations were considered for SEM (see Figure 1): the center of the pellet (center), the periphery of the pellet at mid-height (periphery), the upper extremity of the pellet (top). The evolution of the measured surface porosity with the strain rate is given in Figure 8 for all the temperatures.

The results show that the pore volume at the top and periphery of the samples did not evolve significantly during the tests. There is furthermore no clear trend with strain rate or temperature. Nearly all the measured porosities fall within the standard deviation associated with the pre-test porosity ($2.3\% \pm 0.3\%$). These results are not in contradiction with the previously discussed open porosities from hydrostatic density measurements since macroscopic cracks (size >> grain size) were not considered in the analyses of SEM images.

The picture at the pellet centers is different. Again, most of the porosities also fall within the standard deviation associated with the pre-test porosity of the samples. The porosities measured at the highest strain rate (10^{-1}/s) are however significantly greater than before test (they are not indicated in Figure 8). At 1550°C, it reaches 17%, at 1700°C, 8%. The SEM images obtained at 1350°C, 1550°C and 1700°C are shown in Figure 9. The increase in the measured surface porosity during the tests at 1550 and 1700°C is due to a very pronounced grain boundary cracking at the pellet center with no preferred orientation.

2.4 Temperature - Stress threshold for grain boundary cracking

The test results are summarized in Figure 10. The stresses at 2% strain (after the peak stress) are plotted in function of temperature for the different strain rates (solid lines). The stresses obtained from similar tests performed in a previous study on a UO_2 with 4% initial porosity (average grain size 9 μm) [26] are also recalled in Figure 10. Obviously, a 2% increase in porosity leads to an important decrease of the yield stress in strain-rate controlled compression tests. The stress differences between the two UO_2 materials are furthermore enhanced at low temperature (1100°C). These results confirm that porosity is a parameter of primary importance with respect to the mechanical properties of UO_2 [21, 22].

The stress - temperature - strain rate conditions leading to macroscopic

cracking of the pellets are also indicated in Figure 10 (in blue). The important parameter seems here to be the temperature and to a lesser extent strain rate. Only the samples tested at 1100 and 1350°C showed macroscopic axial cracks after loading. Porosity does not seem to play a significant role on this point since macroscopic cracks appeared in both UO_2 materials.

The stress - temperature - strain rate conditions leading to grain boundary cracking in the pellets are highlighted in Figure 10 (in red). Only the samples tested at the highest strain rates and the highest temperatures showed areas of pronounced grain decohesion. Porosity seems here to be an important parameter since only the dense UO_2 with a 2% porosity led to this type of damage. Similar observations on dense uranium dioxide were reported by Dherbey et al. [15] and Ndiaye [16]. It is worth recalling that only the center of the pellets did exhibit grain boundary cracking. As shown later, this is a consequence of the non homogeneous stress state in the pellet due to friction at pellet ends. The thermo-mechanical conditions leading to grain boundary cracking can thus only be deduced from a more in-depth analysis of the tests, i.e., from an analysis of the stress state at the pellet center.

3 Modeling

3.1 Constitutive model

Salvo and al. [26] have recently proposed a constitutive model for UO_2 that describes the strain-rate and temperature dependency of the material behavior under compressive stresses. To cover a large domain of strain-rates ($10^{-9} - 10^{-1}$/s) and following Dherbey et al. [15], a hyperbolic sine function was used to define the stress sensivity of the viscoplastic strain rate. Based on the work of Monerie and Gatt [29], pore volume compressibility was furthermore included in the formulation. Details on the model derivation can be found in reference [26]. Only the main elements will be recalled hereafter.

The viscoplastic strain rate tensor is given by the following function of the equivalent stress Σ and temperature T:

$$\dot{\boldsymbol{\varepsilon}}^{vp} = K e^{-\frac{Q}{RT}} \sinh\left(\frac{\Sigma}{\sigma_0}\right)\left(\frac{1}{3}\alpha\frac{\sigma_m}{\Sigma}\mathbf{1} + \frac{3}{2}\beta\frac{\boldsymbol{s}}{\Sigma}\right) \tag{4}$$

where K and σ_0 are the main parameters of the model together with the activation energy Q. The equivalent stress $\Sigma = \sqrt{\alpha {\sigma_m}^2 + \beta {\sigma_{eq}}^2}$ is a function of both the hydrostatic stress $\sigma_m = \frac{1}{3}\,\boldsymbol{\sigma} : \mathbf{1}$ and of the second invariant of the stress tensor $\sigma_{eq} = \sqrt{\frac{3}{2}\boldsymbol{s} : \boldsymbol{s}}$ (with $\boldsymbol{\sigma}$ the stress tensor, $\mathbf{1}$ the unit tensor and $\boldsymbol{s} = \boldsymbol{\sigma} - \sigma_m\mathbf{1}$ the deviatoric stress tensor). The two parameters $\alpha(f)$ and $\beta(f)$

define the relative contribution of the hydrostatic σ_m and of the deviatoric stress invariants σ_{eq} to the strain rate. They were identified by analogy with the equivalent stress $\Sigma = \sqrt{\frac{9}{4}A{\sigma_m}^2 + B{\sigma_{eq}}^2}$ used in the compressible model of Monerie and Gatt [29]. The parameters $A(f)$ and $B(f)$ ensure that the incompressible viscoplastic behaviour of the matrix is recovered when the porosity f tends to zero ($A(f) \to 0$ when $f \to 0$ and $B(f) \to 1$ when $f \to 0$). They are given by the following expressions:

$$A(f) = \left(6\left(f^{-\frac{1}{6}} - 1\right)\right)^{-\frac{12}{7}} \tag{5}$$

$$B(f) = \left(1 + \frac{2}{3}f\right)(1-f)^{-\frac{12}{7}} \tag{6}$$

The evolution of the porosity volume fraction f was then defined by the following mass balance equation originally proposed by Monerie and Gatt [29]:

$$\dot{f} = (1-f)\dot{\boldsymbol{\varepsilon}}^{vp} : \mathbf{1} = (1-f)Ke^{-\frac{Q}{RT}}\sinh\left(\frac{\Sigma}{\sigma_0}\right)\alpha\frac{\sigma_m}{\Sigma} \tag{7}$$

Based on the simulation of more than 200 creep tests on uranium dioxide with grain diameter within 4-70 μm, the impact of grain size d was also included in the model with the following expression for the K parameter [26]:

$$K = K_0 \exp\left[-\gamma/(d - d_0)\right] \tag{8}$$

with K_0, γ and d_0 as constant parameters.

3.2 Parameters identification

The determination of the parameters of the model is detailed in reference [26]. A two step process is used. First, based on the simplifying assumption that the stress state in the pellet is close to uniaxial compression and neglecting elastic strains and pore compressibility, a preliminary estimate of the parameters is obtained using a standard Excel spreadsheet with a numerical solver. Under these specific conditions and at constant applied strain rate, the hyperbolic sine model leads a constant stress that is compared to the stresses measured at 2% strain in the tests. The stresses at 2% strain are used as a reference since they are usually situated after the stress peak in the tests and thus do not account for this specific behavior rather unlikely during in-reactor irradiation (the stress peak tends to disappear during loading cycles [30]). Second, a best fit of the parameters is deduced from iterative Finite Element

simulations of the tests. This two-step process, applied to the 4% porosity dioxide uranium tested at the same strain rates and temperatures than the dense material of this study, led to the set of parameters summarized in Table 1. Note that a small evolution of the activation energy with temperature had to be introduced to better match the stress-strain curves at 1100°C.

Applying the hyperbolic sine model with the parameters of Table 1 to the experimental data obtained on the dense UO_2 studied in this work leads to some differences between calculated and measured stresses at 2% strain (see Figure 11 top graph where the stresses are calculated according to the first step described above). A reasonable fit of the data is however obtained with a small variation in σ_0 (6.3 MPa instead of 5 MPa), all other parameters identical. Figure 11 (bottom graph) shows now the good agreement between simulated and measured stresses at 2% strain with the exception of the tests performed at 1100°C (highest measured stresses). The very important stress peak observed at this temperature together with the softening of the stress-strain response renders the determination of a yield stress rather artificial.

In theory, the porosity dependency of the equivalent stress $\Sigma = \sqrt{\alpha {\sigma_m}^2 + \beta {\sigma_{eq}}^2}$ with $\alpha = \frac{9}{4}A(f)$ and $\beta = B(f)$ should lead to some differences in the yield stress of UO_2 materials with 2 and 4% porosity. The dependency is however small and does not lead to the observed increase of stress with the reduction in porosity. One may argue that porosity is not the only important parameter and that the differences between the two UO_2 materials might be related to another parameter, e.g., grain size, pore shape, ... There is however strong evidence that porosity plays a major role in UO_2 and in ceramics in general [31, 32]. Igata et Domoto observed at room temperature an exponential decrease of the compressive strength with porosity [21]. Radford and Oguma related the room temperature bending strength of different UO_2 to their porosity using also an exponential function [22] [24]. The importance of porosity on bending strength was also confirmed at high temperatures (up to 1800°C) by Roberts and Ueda [23] and Armstrong et al. [33]. Experimental data concerning the impact of porosity on the compressive strength of UO_2 at high temperatures are however scarce.

To enhance the porosity dependency of the model without loosing the physics behind pore compressibility (driven by the hydrostatic stress [34]), the porosity-dependent parameters α and β have been modified as follows:

$$\alpha(f) = \beta(f)\frac{A(f)}{B(f)} \tag{9}$$

$$\beta(f) = \frac{B(f) + 20A(f)}{B(f)} \tag{10}$$

The basic properties of the equivalent stress proposed by Monerie and Gatt in their compressible creep model still hold: the incompressible viscoplastic behaviour of the matrix is recovered when the porosity f tends to zero ($\alpha(f) \to 0$ when $f \to 0$ and $\beta(f) \to 1$ when $f \to 0$). The factor 20 in Equation 10 was chosen to reproduce the observed differences in stresses between the 2 and 4% porosity UO_2 materials. The final set of parameters deduced from the Finite Element simulations of the tests performed on these two uranium dioxide materials are now summarized in Table 2.

Since the database considered to adjust the porosity-dependency of the model is limited, its response was compared to measurements of other authors. The evolution of the calculated compressive yield stress with porosity at different temperatures and for a strain rate of 5.10^{-6}/s is plotted in Figure 12. The model is compared to the room temperature measurements of Igata [21] (porosity 2 to 9%, grain size ~ 10 μm, strain rate $\sim 10^{-6}$/s) and to that of an internal CEA study [35] (temperature 1450°C, porosity 1 to 8%, grain size $8-15$ μm, strain rate $\sim 10^{-5}$/s). Figure 12 shows the huge variation in the compressive yield stress of UO_2 with temperature (over 3 orders of magnitude). In comparison, the evolution with porosity appears small. The dependency to both these parameters is correctly reproduced by the model, at least within the scatter of the measured stresses.

3.3 Constitutive model for grain boundary cracking

Assuming again that the compression test leads to a uniform stress state in the samples, Equation 7 reduces to:

$$\dot{f} = -(1-f)K\frac{\alpha}{\sqrt{\frac{1}{9}\alpha+\beta}}e^{-\frac{Q}{RT}}\sinh\left(\frac{\sigma\sqrt{\frac{1}{9}\alpha+\beta}}{\sigma_0}\right) < 0 \qquad (11)$$

Obviously, during a compression test, and according to the proposed hyperbolic sine model, the porosity can only decrease. It was shown in a previous paper that porosity contraction takes place during loading of a sufficiently porous UO_2 (4% initial porosity) [26]. In the present study, no significant reduction of the pore volume was observed after the tests, whatever the temperature, strain rate or strain level. It even appeared that the porosity and sample volume had increased during some of the tests. The latter phenomenon has been related to macroscopic axial cracking of the samples or to grain boundary cracking. The modeling of macroscopic cracking during compression tests will not be discussed here since it requires sophisticated approaches that are beyond the goals of this paper [36]. Grain boundary

cracking will however be considered in this work since it can be treated at the scale of the material, i.e., at the scale of the Representative Elementary Volume (REV).

According to Bazant [37], there are three possible mechanisms at the microscale triggering compression fracture in quasi-brittle materials: pores can cause tensile splitting microcracks to grow from the pores under a compression load, stiff inclusions can produce short tensile splitting microcracks below and above the inclusions, weak inclined interfaces between crystals can cause the growth of curved cracks called wing-tip cracks. It is important to emphasize that all these mechanisms lead to short cracks of the same order of magnitude as the pore diameter, inclusion or crystal size. They result therefore in a distributed damage that is macroscopically smeared.

In a previous experimental study, it was shown that excess porosity at the grain boundary does not induce significant microcracking during compression tests [26] but rather accommodates the grains' deformation. The SEM pictures of Figure 9 show that grain boundary cracking in the 2% porosity samples is relatively homogeneous and closely related to the crystals or grains distribution. The relation between grain boundaries orientation and the development of microcracks has been assessed by micromechanical numerical simulations of UO_2 with however no modeling of the pores at the grain boundaries [17, 18]. It was found that strain incompatibilities between the grains can lead locally to tensile stresses exceeding the tensile strength of UO_2 ($\sim$ 100 MPa) with maximum at the interface between grains orientated at an angle of 0 to 45° with respect to the loading direction.

In quasi-brittle materials, plasticity-based models are often used to model micro-cracking in compression [38]. Upon them, the Drucker-Prager yield criterion provides a simple means of accounting for the hydrostatic pressure dependency of the yield strength and for the associated volume expansion. The Drucker-Prager criterion has been applied to metals, plastics and soils [39, 40]. It has also been used to describe the plastic deformation of grain boundaries in nano-grained ceramics [41]. In this paper, the strains associated to grain boundary cracking will be averaged at the macroscopic scale using a Drucker-Prager yield criterion of the following form:

$$g(\boldsymbol{\sigma}) = \omega\sigma_m + \sigma_{eq} - \sigma_{gbc} \leq 0 \tag{12}$$

with ω and σ_{gbc} two positive material parameters. The plastic yield criterion depends on the hydrostatic pressure σ_m and on the second invariant of the stress tensor, σ_{eq}. Associated plasticity is considered such that the plastic strain rate tensor $\dot{\boldsymbol{\varepsilon}}^p$ is defined by:

$$\begin{cases} \dot{\boldsymbol{\varepsilon}^p} = \dot{\lambda}\dfrac{\partial g}{\partial \boldsymbol{\sigma}} \ \text{ if } \ g(\boldsymbol{\sigma}) = 0 \\ \dot{\boldsymbol{\varepsilon}^p} = 0 \ \text{ if } \ g(\boldsymbol{\sigma}) < 0 \end{cases} \tag{13}$$

$\dot{\lambda} \geq 0$ is the plastic multiplier which can be obtained from the consistency conditions $\dot{g} = 0$. The dilatancy associated with grain boundary cracking is here related to the plastic strains by:

$$\dot{f} = (1 - f)\ \dot{\boldsymbol{\varepsilon}^p} : \mathbf{1} = (1 - f)\omega > 0 \tag{14}$$

Equation (14) shows that the porosity of UO_2 can only increase with grain boundary cracking. The variation in porosity due to plastic flow is often referenced as plastic porosity [40].

3.4 Grain boundary cracking parameters identification

The two parameters of the Drucker-Prager yield criterion ω and σ_{gbc} are obtained by considering uniaxial tensile and compressive tests. In tension, $\sigma_{zz} = \sigma_t$, in compression, $\sigma_{zz} = -\sigma_c$ with σ_t and σ_c respectively as the stress thresholds at which grain boundary cracking starts. Simple algebraic manipulation leads to the following expression for σ_{gbc}:

$$\sigma_{gbc} = 2\frac{\tau}{1 + \tau}\sigma_c \tag{15}$$

where $\tau = \sigma_t/\sigma_c$. The parameter σ_{gbc} in Equation 15 is proportional to the uniaxial compressive stress σ_c at which grain boundary cracking starts. From Figure 10, it is obvious that the grain boundary cracking stress threshold decreases with increasing temperature. At temperatures below 1350°C, macroscopic cracking is predominant and the criterion should therefore not be reached. The determination of a suitable function for $\sigma_c(T)$ is further complicated by the fact that grain boundary cracking took place only at the pellet center. The proposed function is based on the exact stress state at the pellet center obtained from Finite Element simulations of the tests, see Section 4.1. An exponential decreasing function of temperature of the following form was thus defined:

$$\sigma_c(T) = \exp\left[4.10^{-7}T^2 - 2.55\,10^{-3}T + 8\right] \tag{16}$$

with T in K and σ_c in MPa. The function was chosen to ensure that the (three-dimensional) stress state calculated at the pellet center during the

tests performed at 10^{-1}/s and 1550-1700°C exceeded the Drucker-Prager yield criterion ($g(\boldsymbol{\sigma}) \geq 0$). Below 1550°C, it was assumed that macroscopic cracks develop before grain boundary cracking and hence that the stress state did not reach the Drucker-Prager criterion ($g(\boldsymbol{\sigma}) < 0$). The compressive stress function σ_c for grain boundary cracking is plotted in Figure 13 in function of temperature. The FE calculated stresses at the pellet center during the tests performed at 10^{-1}/s are also indicated. As expected, the grain boundary yield stress is reached at 1550°C and 1700° but not at 1350°C and 1100°C.

The parameter ω can be related to the ratio τ between the uniaxial compressive stress and the uniaxial tensile stress at which grain boundary cracking has been observed:

$$\omega = \frac{1-\tau}{1+\tau} \tag{17}$$

In the bending tests of Canon [12], failure of the samples was brittle and characterized by intra-granular cracking up to a so-called transition temperature. Failure then became ductile with high strains and evidence of pronounced grain boundary cracking. The transition temperature was found dependent on the strain rate, equal to approximately 1600°C at 10^{-3}/s. The tensile stress at the brittle to ductile transition temperature was close to 100 MPa. There is therefore experimental evidence that grain boundary cracking in tension can also be associated with a temperature-stress threshold. The precise determination of the ratio τ would require an experimental campaign combining bending and compression tests. In the present work, it was assumed that grain boundary cracking in tension occured at a slightly lower stress level than in compression. A constant value of 0.9 for τ was considered, independent of temperature. This choice leads to $\omega \sim 0.15$ and thus to a small dilatancy ($\sim 0.15\%$ per % axial plastic strain).

3.5 Numerical implementation

The hyperbolic sine and Drucker-Prager plasticity models were readily implemented using a code generator called MFront which is developed by the CEA. MFront allows the user to write constitutive equations in a way which is very similar to their mathematical expressions, notably by providing an appropriate tensorial formalism [42]. MFront turns the user's behaviour implementation into optimised C++ sources which can be plugged into several mechanical solvers. The simulations reported in this paper were performed using Cast3M, the CEA finite element solver [43].

The constitutive equations are written using the standard small-strain formalism based on an additive partitioning of the total strain into an elastic, a plastic and a viscoplastic part:

$$\boldsymbol{\sigma} = \boldsymbol{C} : \boldsymbol{\varepsilon}^e = \boldsymbol{C} : (\boldsymbol{\varepsilon} - \boldsymbol{\varepsilon}^{vp} - \boldsymbol{\varepsilon}^p) \tag{18}$$

where $\boldsymbol{C}$ is the fourth order elastic tensor and $\boldsymbol{\varepsilon}^e$ the elastic strain tensor. An implicit numerical scheme is used to solve the system with the main unknowns as the six components of the elastic strain tensor, the equivalent viscoplastic strain defined by $\boldsymbol{\varepsilon}^{vp} : \boldsymbol{\varepsilon}^{vp}$, the equivalent plastic strain $\boldsymbol{\varepsilon}^p : \boldsymbol{\varepsilon}^p$ and the porosity f. The evolution of porosity is given as follows in function of viscoplastic and plastic strains:

$$\dot{f} = \dot{f^p} + \dot{f^{vp}} = (1-f)\dot{\boldsymbol{\varepsilon}}^p : \mathbf{1} + (1-f)\dot{\boldsymbol{\varepsilon}}^{vp} : \mathbf{1} \tag{19}$$

The system of Equations 4, 12, 13, 18 and 19 has been solved in finite strain computations using a hypoelastic eulerian formulation provided by the Cast3M finite element solver. Cast3M implementation is close to the one described by Simo and Hugues [44].

4 Finite Elements simulations

4.1 Simulation of strain driven tests

As discussed in Section 2, the stress state in the samples tested in compression is far from being uniaxial. Friction at the upper and lower ends tends to generate a three-dimensional stress state. The important axial and hoop strains reached during the tests suggest that structural non linearities (large displacements) might be of importance when analysing the results.

The mesh and boundary conditions used in the simulations are presented in Figure 14. Only half of the pellet is meshed with quadratic elements assuming two-dimensional axisymmetry. The upper and lower tungsten plates are not directly taken into account. The strong friction at pellet ends is described by the boundary conditions: the radial displacement of the upper and lower surface is forbidden. A constant axial displacement rate between 0.01 and 100 mm/s (depending on the test simulated) is then prescribed on the upper surface of the pellet. The maximum prescribed axial displacement matches the experimental value to ease the comparison of residual strains. The thermal strains are taken into account prior to the displacement-driven phase. They are substracted at the end of the simulation.

The modulus of elasticity E and Poisson ratio ν considered in the simulations are based on Martin et al. [45]. They are expressed in function of the

temperature T (in K) and of the porosity f as follows:

$$E = (1 - 2.5f)(226.93 - 1.5399 \times 10^{-2}T - 9.597 \times 10^{-6}T^2) \quad (20)$$

E is given in GPa. ν is constant and equal to 0.3. The initial porosity of uranium dioxide considered in the simulations was based on the average relative density measured prior to testing: $f_0 = 0.019$.

All the simulated and measured stress-strain curves are presented in Figure 15. Two simulations of each tests were performed. One with the Drucker-Prager plastic criterion, one without. The model reproduces correctly the strain rate and temperature dependency at moderate strain level (a few %), i.e., the increase or decrease of the stress with temperature and strain rate. The largest differences are observed in the tests performed at 1100°C which presented macroscopic axial cracks on the periphery of the samples. In particular, the post-peak softening behavior at 1100°C is not reproduced. The apparent strain hardening during the other tests is partly recovered in the simulations (due to the change of geometry of the samples mainly) but generally underestimated. Material plastic hardening not taken into account in the model could be of importance here.

The activation of the Drucker-Prager plastic criterion does not lead to major changes in the stress-strain curves. As expected, the criterion is only reached at the highest strain rate and at the temperatures of 1550 and 1700°C. In consequence, the stress level given by the Drucker-Prager yield criterion is slightly lower than predicted by the hyperbolic sine model (see the small difference between the blue and red curves in the bottom left graphs of Figure 15).

In a similar way, all the post-test diameter profiles of the samples are compared in Figure 16 to the simulations results with and without the Drucker-Prager criterion. A good agreement is obtained for all the tests except at 1100°C where pronounced cracking led to chaotic diameter profiles. The addition of grain boundary cracking in the simulations leads to a small additional diameter increase in the central part of the samples where the yield criterion is reached (10^{-1}/s, 1550 and 1700°C), see the difference between the blue and red curves in the bottom left graphs of Figure 16.

The calculated evolution of the porosity in the tests is given in Figure 17. The experimental trend (Figure 8) is well reproduced by the simulations since no significant pore volume variation is obtained. Grain boundary cracking leads, in the test at 1700°C and 10^{-1}/s, to an increase of the initial porosity (+0.3%) at the pellet center. The reason for that localization of plastic porosity can be explained by the inhomogeneity of the stress state in the samples. Figure 18 shows the axial (σ_{zz}) and equivalent stress (σ_{eq})

distribution during the test at 1550°C and 10^{-1}/s. Pronounced axial and to a lesser extent radial gradients of stress are obviously at hand. The stresses are maximum at the pellet center where the Drucker-Prager yield criterion is first exceeded. The maximum equivalent plastic strain reaches 4% at the sample core.

Without the Drucker-Prager plastic criterion and in consequence of the stress state, the simulation leads to a decrease of the pore volume near the pellet center (see f_{pv} in Figure 18 with a minimum $\sim 1.2\%$ or the triangles in Figure 17). On the contrary, an increase of the porosity is observed when plastic flow is activated (see f_p in Figure 18 with a maximum around 0.6%). The porosity in the simulation being the sum of the plastic and viscoplastic contributions, it is finally fairly constant at the end of the test and at the sample core (see the circles in Figure 17). It has furthermore not changed greatly at the pellet top since lower stresses are at hand in this region.

The calculated porosity increase is of course far from the 8 to 17% measured locally from the SEM images. It may be due to the limited extension in space of grain boundary cracking. Our simulations are based on macroscopic average strains that probably do not reflect the strain localization associated with grain boundary cracking. In fact, the diameter profiles which are characteristic of the average volume increase of the material are fairly well reproduced by the simulation.

4.2 Biaxial Compression Stress Plane

During RIA power transients, the stress state in the pellet is closer to equibiaxial compression than to uniaxial compression [4]. It is therefore of some interest to study the response of the hyperbolic sine creep and Drucker-Prager plastic models in case of a compression loading with different stress or strain biaxiality ratios.

The simulations were performed on a single cubic element of unit length with prescribed displacement rates in two perpendicular directions such that $\dot{\epsilon}_{eq} = \sqrt{\dot{\epsilon}_{yy}^2 + \dot{\epsilon}_{zz}^2} = 1$/s or 10/s. The simulations were made at constant temperatures ranging from 1000 to 2600°C by step of 200°C. The calculated yield stresses are plotted in Figures 19 and 20 for equivalent strain rates of 1/s and 10/s, respectively.

In equibiaxial compression, the yield stress ($\sigma_{yy} = \sigma_{zz} = \sigma_{bc}$) is very close to its uniaxial counterpart (σ_c). The biaxial to uniaxial compressive stress ratio (σ_{bc}/σ_c) does furthermore not evolve with temperature and strain rate. This is a major result that stems from the creep-grain boundary cracking constitutive model developed in this paper. It cannot be checked because of the lack of experimental data on UO_2 under biaxial loading conditions.

The origin of the yield stresses plotted in Figures 19-20 is either viscoplastic flow or plastic flow (grain boundary cracking). The distinction is highlighted by using a colour code such that dark lines represent viscoplastic limits (creep flow) and bright lines plastic limits (grain boundary cracking). The brighter the line, the greater the contribution of plastic strains to the total strain. Obviously, at an equivalent strain rate of 1/s, both mechanisms are active over the whole range of temperatures. Only at the lowest and highest temperatures (< 1600°C and > 2400°C) does the viscoplasticity of UO_2 become dominant. In-between and as temperature increases, plastic strains contribute more and more to the total strain. The picture is different at 10/s since most of the stress-high temperature domain is controled by plasticity. The deleterious impact of strain rate is therefore obvious when comparing Figures 19 and 20. Increasing the strain rate tends to increase the temperature domain where plastic flow controls the stresses, i.e., where grain boundary cracking might take place.

According to the model, it appears furthermore that the mechanism at the origin of the yield stress does not depend significantly on the stress ratio. If the uniaxial compressive stress is controled by viscoplastic flow, then the biaxial compressive stress is also. It can therefore be expected that at a similar temperature and strain rate, a biaxial compressive stress state will lead to grain boundary cracking if it has been observed in a uniaxial compression test.

Conclusions

In this paper, the behavior of a dense UO_2 (porosity less than 2%) was studied experimentally on a range of temperatures (1100°C - 1700°C) and strain rates ($10^{-4} - 10^{-1}$/s) representative of RIA loading conditions. The yield stress was found to increase with strain rate and to decrease with temperature. Macroscopic cracking of the samples was apparent after the tests at 1100°C which was consistent with the monitoring of stress-strain softening. SEM image analyses revealed a pronounced grain boundary cracking in the core of the samples tested at 10^{-1}/s and at 1550-1700°C.

Compared to previous test results obtained in similar conditions but on a more porous UO_2 (4%), these experimental results show the importance of porosity on the potential damage of grain boundaries. A hyperbolic sine model for the viscoplastic strain rate with a clear dependency on porosity was thus developed. It was completed by a Drucker-Prager yield criterion with associated plastic flow to account for the (macroscopic) porosity increase induced by grain boundary cracking.

Finite Elements simulations of the compression tests on the dense UO_2

were then successfully compared to the stress-strain curves, post-test diameter profiles and porosities at the pellets' center, periphery and top extremity. The response of the grain boundary cracking macroscopic model based on the Drucker-Prager yield criterion was then studied in biaxial compression, this condition being closer to that of the pellet during a RIA power transient.

It may be emphasized that the determination of the grain boundary cracking model is based on a very limited number of tests performed solely in uniaxial compression. Tests in biaxial loading conditions (compression and tension) would be necessary to fully assess the response of the model in RIA simulation.

The proposed model will be implemented in the fuel performance code ALCYONE-RIA [5] and coupled with a suitable smeared crack model to describe pellet cracking in tension.

References

[1] J. Papin, B. Cazalis, J. M. Frizonnet, J. Desquines, F. Lemoine, V. Georgenthum, F. Lamare, and M. Petit. Summary and interpretation of the CABRI REP-Na program. *Nuclear Technology*, 157(3):230–250, 2007.

[2] T. Fuketa, H. Sasajima, and T. Sugiyama. Behavior of high-burnup PWR fuels with low-tin zircaloy-4 cladding under reactivity-initiated-accident conditions. *Nuclear technology*, 133(1):50–62, 2001.

[3] L. Yegorova, K. Lioutov, N. Jouravkova, O. Nechaeva, A. Salatov, V. Smirnov, A. Goryachev, V. Ustinenko, and I. Smirnov. Experimental study of narrow pulse effects on the behavior of high burnup fuel rods with Zr-1%Nb cladding and UO_2 fuel (VVER type) under reactivity-initiated accident conditions: Program approach and analysis of results. Technical Report NUREG/IA-0213, Vol. 1, U.S. Nuclear Regulatory Commission, May 2006.

[4] M. Suzuki, T. Sugiyama, and T. Fuketa. Thermal stress analysis of high-burnup LWR fuel pellet pulse-irradiated in reactivity-initiated accident conditions. *Journal of Nuclear Science and Technology*, 45(11):1155–1164, 2008.

[5] J. Sercombe, E. Fédérici, M. Le Saux, B. Michel, and C. Poussard. 1D and 3D modeling of PCMI during a RIA with ALCYONE V1.1. In *TopFuel 2010*, Orlando, Florida, USA, 2010.

[6] F. Schmitz and J. Papin. High burnup effects on fuel behaviour under accident conditions: the tests CABRI REP-Na. *Journal of Nuclear Materials*, 270(1–2):55–64, April 1999.

[7] F. Lemoine. High burnup fuel behavior related to fission gas effects under reactivity initiated accidents (RIA) conditions. *Journal of Nuclear Materials*, 248:238–248, 1997.

[8] A. Moal, V. Georgenthum, and O. Marchand. Scanair: A transient fuel performance code: Part one: General modelling description. *In Press, Nuclear Engineering and Design*, 2014.

[9] L. Noirot. Margaret: A comprehensive code for the description of fission gas behavior. *Nuclear Engineering and Design*, 241(6):2099–2118, 2011.

[10] M. Suzuki, Y. Udagawa, T. Sugiyama, and F. Nagase. Model development and verifications for fission gas inventory and release from high

burnup PWR fuel during simulated RIA experiment in NSRR. In *Top Fuel*, Manchester, UK, September 2012.

[11] J.F. Byron. Yield and flow of polycrystalline uranium dioxide. *Journal of Nuclear Materials*, 27(1):48–53, 1968.

[12] R. F. Canon, J. T. A. Roberts, and R. J. Beals. Deformation of UO2 at high temperatures. *Journal of the American Ceramic Society*, 54(2):105–112, 1971.

[13] J.T.A Roberts. Mechanical equation of state and high-temperature deformation (>=0.5Tm) of uranium dioxide. *Acta Metallurgica*, 22(7):873–878, July 1974.

[14] G.L. Reynolds, B. Burton, and M.V. Speight. Creep fracture processes in uranium dioxide. *Acta Metallurgica*, 23(5):573–577, 1975.

[15] F. Dherbey, F. Louchet, A. Mocellin, and S. Leclercq. Elevated temperature creep of polycrystalline uranium dioxide: from microscopic mechanisms to macroscopic behaviour. *Acta Materialia*, 50(6):1495–1505, April 2002.

[16] A. Ndiaye. *Combustible nucléaire UO2 à microstructures pilotées: compréhension des mécanismes d'élaboration et du comportement mécanique en température*. PhD thesis, Université de Grenoble, France, 2012.

[17] J. Pacull. *Modèle numérique micro-mécanique d'agrégat polycristallin pour le comportement des combustibles oxydes*. PhD thesis, Université de Provence-Aix-Marseille I, 2011.

[18] B. Michel, T. Helfer, J. Soulacroix, M. Salvo, and J. Sercombe. Microfissuration induite par la viscoplasticité dans les céramiques nucléaires. In *Matériaux 2014*, Montpellier, France, 2014.

[19] T. Tachibana, H. Furuya, and M. Koizumi. Dependence on strain rate and temperature shown by yield stress of uranium dioxide. *Journal of Nuclear Science and Technology*, 13(9):497–502, 1976.

[20] Y. Guérin. Etude par compression à hautes températures de la déformation plastique du bioxyde d'uranium polycristallin. *Journal of Nuclear Materials*, 56(1):61–75, April 1975.

[21] N. Igata and K. Domoto. Fracture stress and elastic modulus of uranium dioxide including excess oxygen. *Journal of Nuclear Materials*, 45(4):317–322, 1973.

[22] K.C. Radford. Effect of fabrication parameters and microstructure on the mechanical strength of UO_2 fuel pellets. *Journal of Nuclear Materials*, 84:222–236, 1979.

[23] J.T.A. Roberts and Y. Ueda. Influence of porosity on deformation and fracture of UO2. *Journal of the American Ceramic Society*, 55(3):117–124, 1972.

[24] M. Oguma. Microstructure effects on fracture strength of UO2 fuel pellets. *Journal of Nuclear Science and Technology*, 19(12):1005–1014, 1982.

[25] P. Werner and J.L. Routbort. Effect of pore shape on the fracture of UO_2 up to high strain rates. *Journal of Nuclear Materials*, 113:118–121, 1983.

[26] M. Salvo, J. Sercombe, J. Julien, T. Helfer, and T. Désoyer. Experimental study and modeling of UO_2 behaviour at high strain rates and temperatures. *In Press, Journal of Nuclear Materials*, 2014.

[27] F. Sauter and S. Leclercq. Modeling of the non-monotonous viscoplastic behavior of uranium dioxide. *Journal of Nuclear Materials*, 322(1):1–14, October 2003.

[28] P. Rossi, F.-J. Ulm, and F. Hachi. Compressive behavior of concrete: physical mechanisms and modeling. *Journal of engineering mechanics*, 122(11):1038–1043, 1996.

[29] Y. Monerie and J.-M. Gatt. Overall viscoplastic behavior of non-irradiated porous nuclear ceramics. *Mechanics of Materials*, 38(7):608–619, July 2006.

[30] M. Salvo. *Experimental study and modeling of UO_2 behaviour at high strain rates and temperatures (In French).* PhD thesis, Université d'Aix Marseille, France, 2014.

[31] E. Ryshkewitch. Compression strength of porous sintered alumina and zirconia. *Journal of the American Ceramic Society*, 36(2):65–68, 1953.

[32] J. Zhou, Y. Li, R. Zhu, and Z. Zhang. The grain size and porosity dependent elastic moduli and yield strength of nanocrystalline ceramics. *Materials Science and Engineering*, 445 - 446:717 – 724, 2007.

[33] W.M. Armstrong, W.R. Irvine, and R.H. Martinson. Creep deformation of stoichiometric uranium dioxide. *Journal of Nuclear Materials*, 7(2):133–141, 1962.

[34] J. C. Michel and P. Suquet. The constitutive law of nonlinear viscous and porous materials. *Journal of the Mechanics and Physics of Solids*, 40(4):783–812, May 1992.

[35] V. Basini and A. Mocellin. Internal report, CEA, Cadarache, 2001.

[36] J. Soulacroix, B. Michel, J.-M. Gatt, R. Kubler, and L. Barrallier. An aging elasto-viscoplastic model for ceramics. *International Journal of Plasticity*, 62(0):121 – 137, 2014.

[37] Z.P. Bazant and J. Planas. *Fracture and size effect in concrete and other quasibrittle materials*. CRC press, 1997.

[38] P.H. Feenstra and R. De Borst. A composite plasticity model for concrete. *International Journal of Solids and Structures*, 33(5):707–730, 1996.

[39] D.C. Drucker. Plasticity theory strength-differential (sd) phenomenon, and volume expansion in metals and plastics. *Metallurgical Transactions*, 4(3):667–673, 1973.

[40] O. Coussy and F. Ulm. *Mechanics of porous continua*, volume 1016. Wiley Chichester, 1995.

[41] B. Jiang and G.J. Weng. A theory of compressive yield strength of nanograined ceramics. *International Journal of Plasticity*, 20(11):2007–2026, 2004.

[42] Thomas Helfer, Eric Brunon, Etienne Castelier, Alain Ravenet, and Nathalie Chauvin. The fuel performance code Celaeno, conception and simulation of fuel elements for gas-cooled fast reactor. In *GLOBAL 2009*, Paris, France, 2009.

[43] Cast3m. http://www-cast3m.cea.fr, 2010.

[44] J.C. Simo and T.J.R. Hughes. *Computational inelasticity*. Springer, New York, 1998.

[45] D.G. Martin. The elastic constants of polycrystalline UO2 and (U, Pu) mixed oxides: a review and recommendations. *High Temperatures. High Pressures*, 21(1):13–24, 1989.

Table 1: Parameters of the compressible hyperbolic sine model of [26].

K_0 (/s)	77400
γ (μm)	5.277
d_0 (μm)	4.6
Q (kJ/mol)	$\max(482; 876 - 0.24T)$
σ_0 (MPa)	5

Table 2: Modified set of parameters for the compressible hyperbolic sine model with α and β given by equations 9 and 10.

K_0 (/s)	77400
γ (μm)	5.277
d_0 (μm)	4.6
Q (kJ/mol)	482
σ_0 (MPa)	7.5

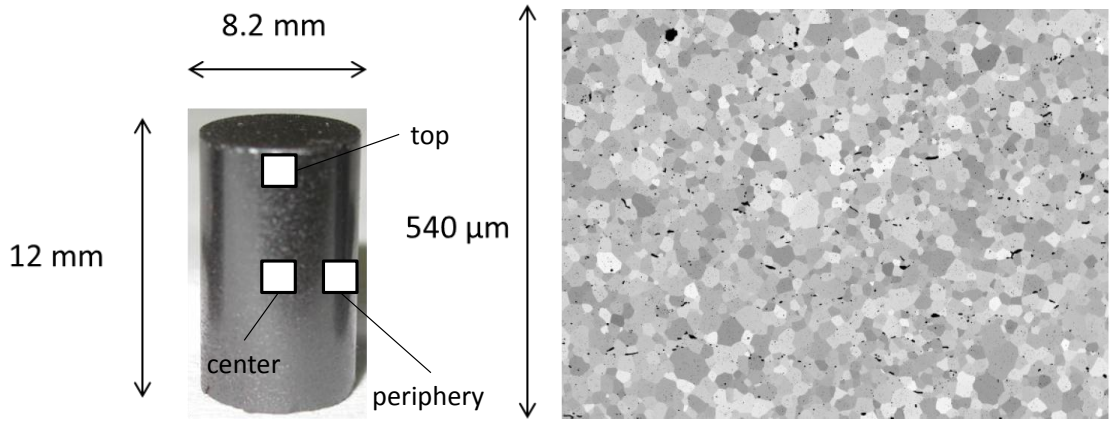

Figure 1: Geometry of the samples and microstructure before testing (SEM).

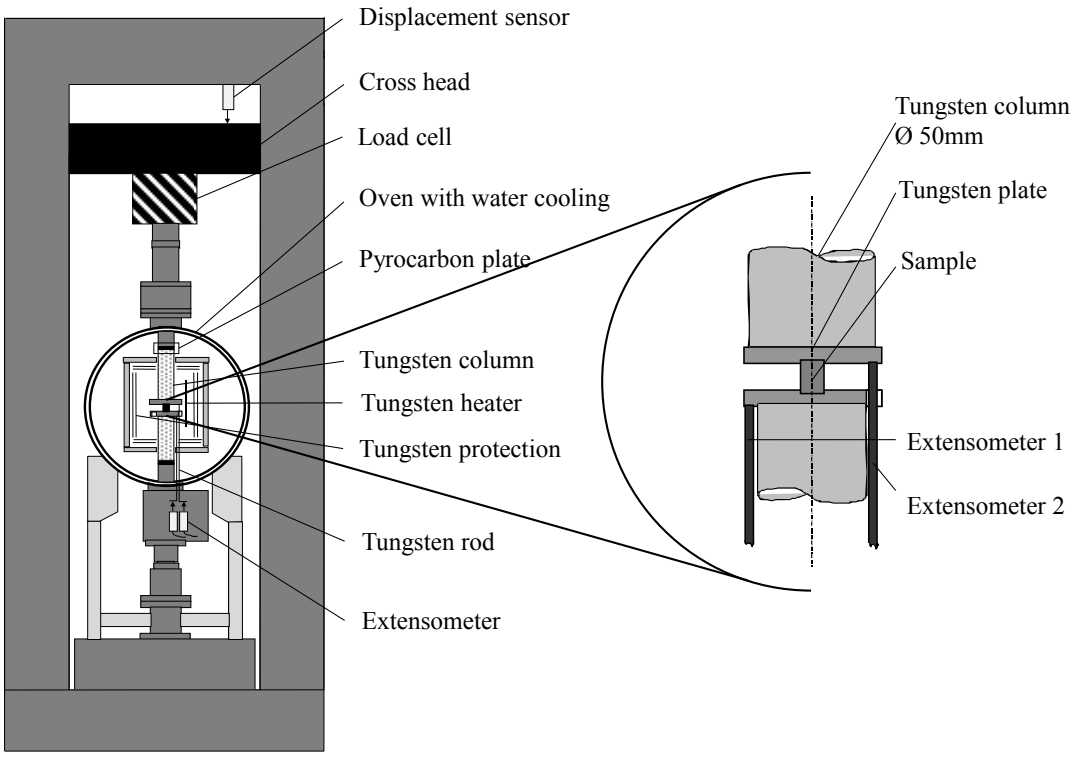

Figure 2: Schematic representation of the testing equipment.

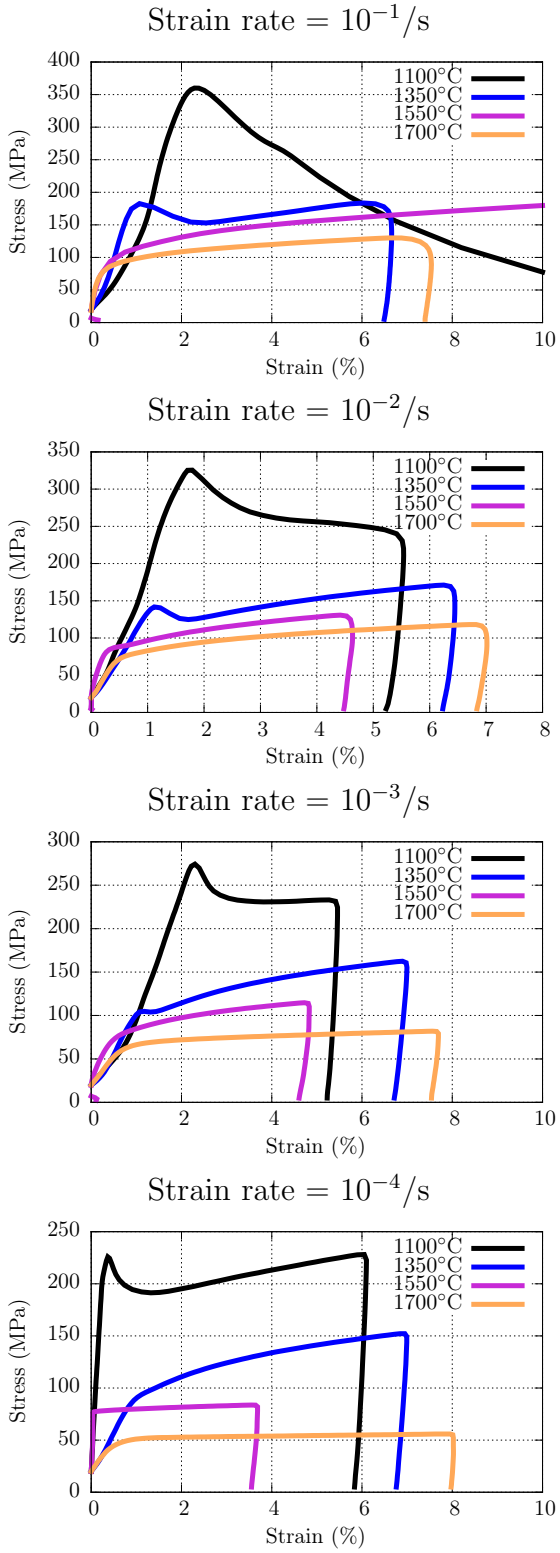

Figure 3: Stress - true strain curves obtained at different strain rates.

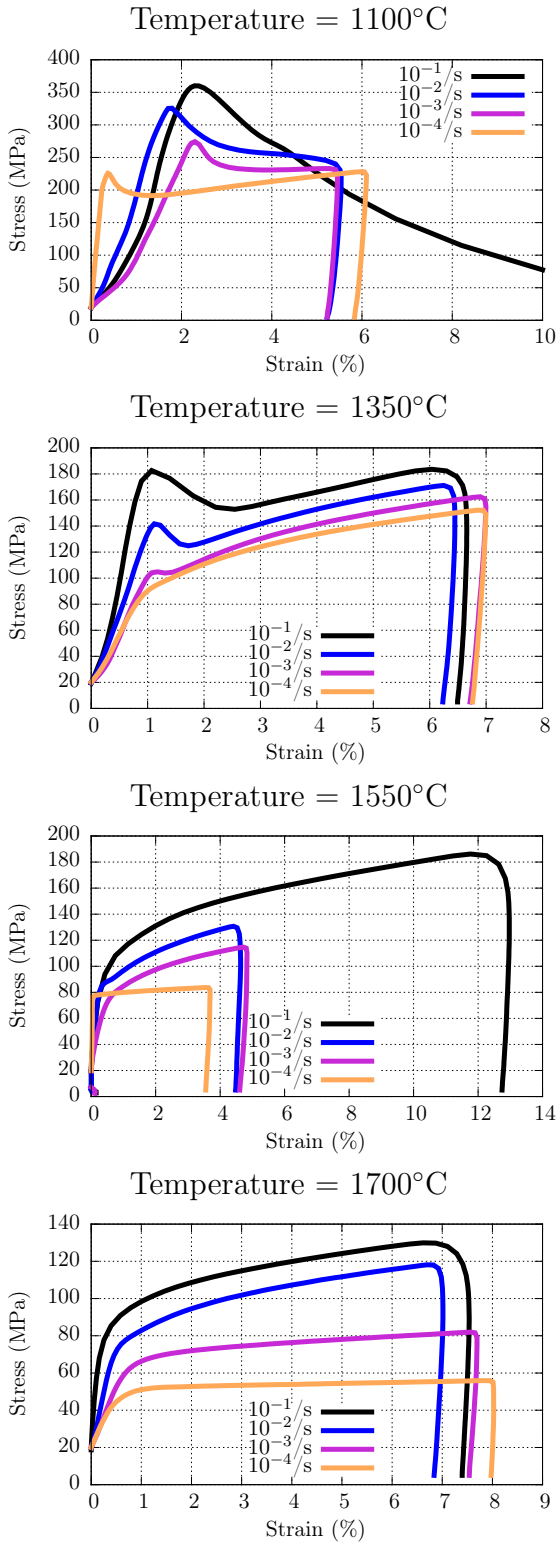

Figure 4: Stress - true strain curves obtained at different temperatures.

Figure 5: Shape of the samples after the tests.

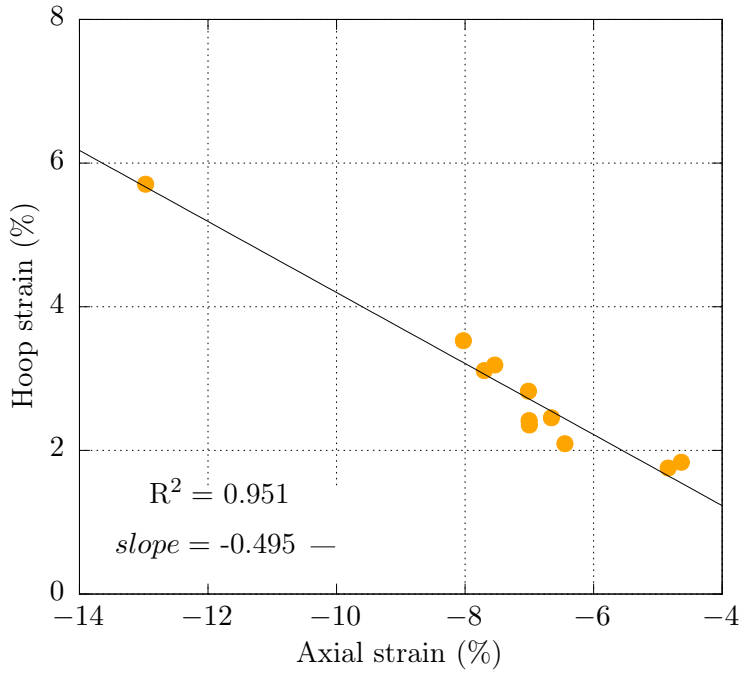

Figure 6: Average residual hoop strains versus residual axial strains (all tests except at 1100°C).

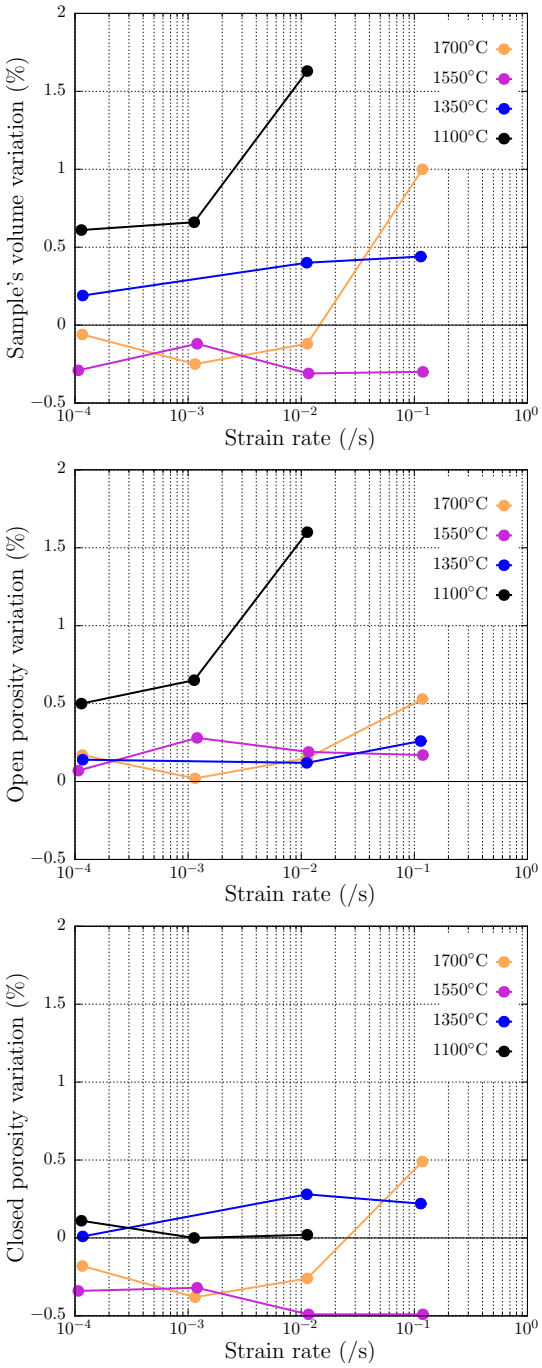

Figure 7: Evolution with temperature and strain rate of the samples' volume (top), open porosity (center), and closed porosity (bottom).

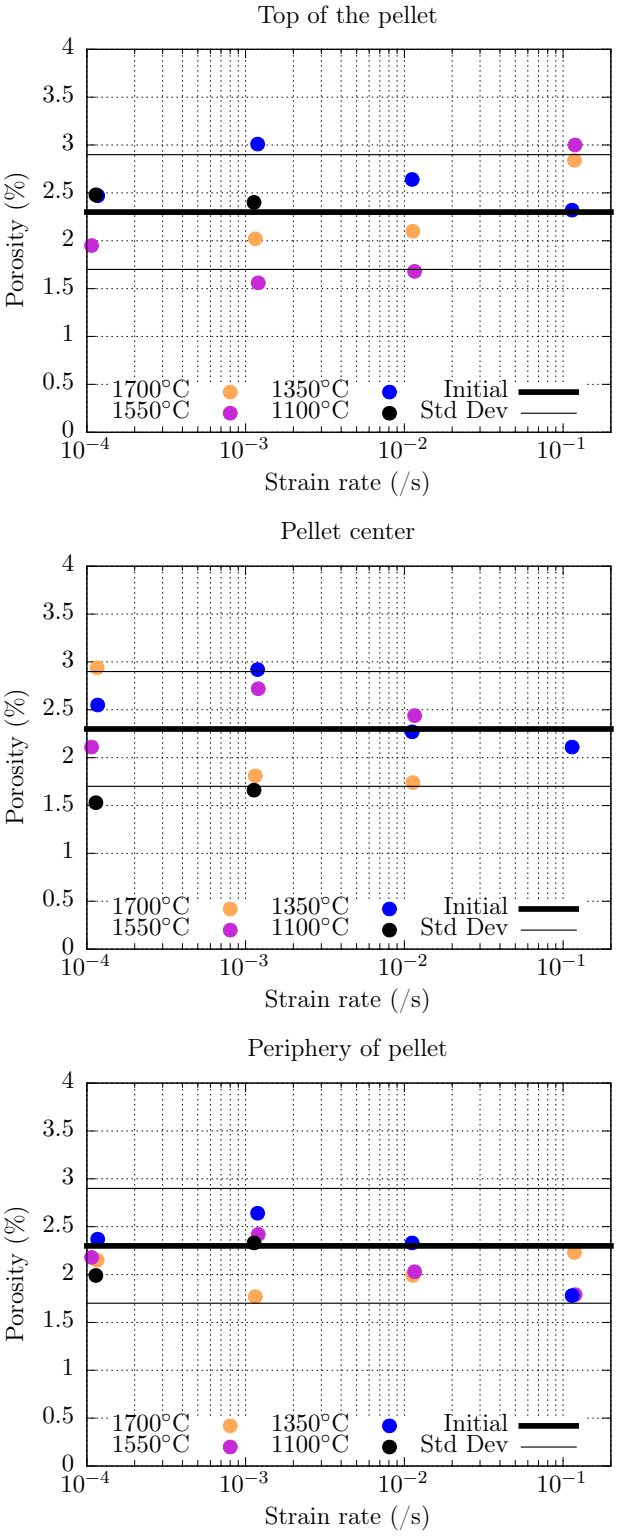

Figure 8: Post-test surface porosities at the top, periphery and center of the samples.

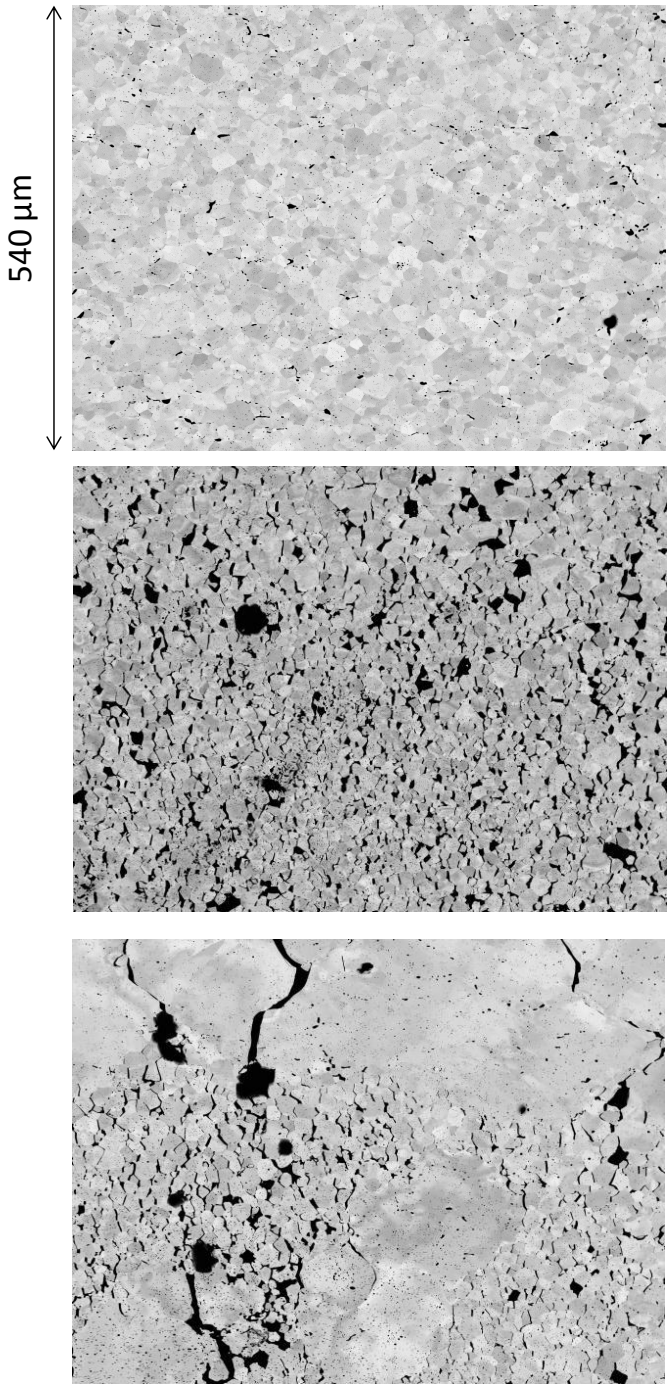

Figure 9: SEM images of the pellet center after testing at 10^{-1}/s and 1350°C(top), 1550°C(middle) and 1700°C(bottom)

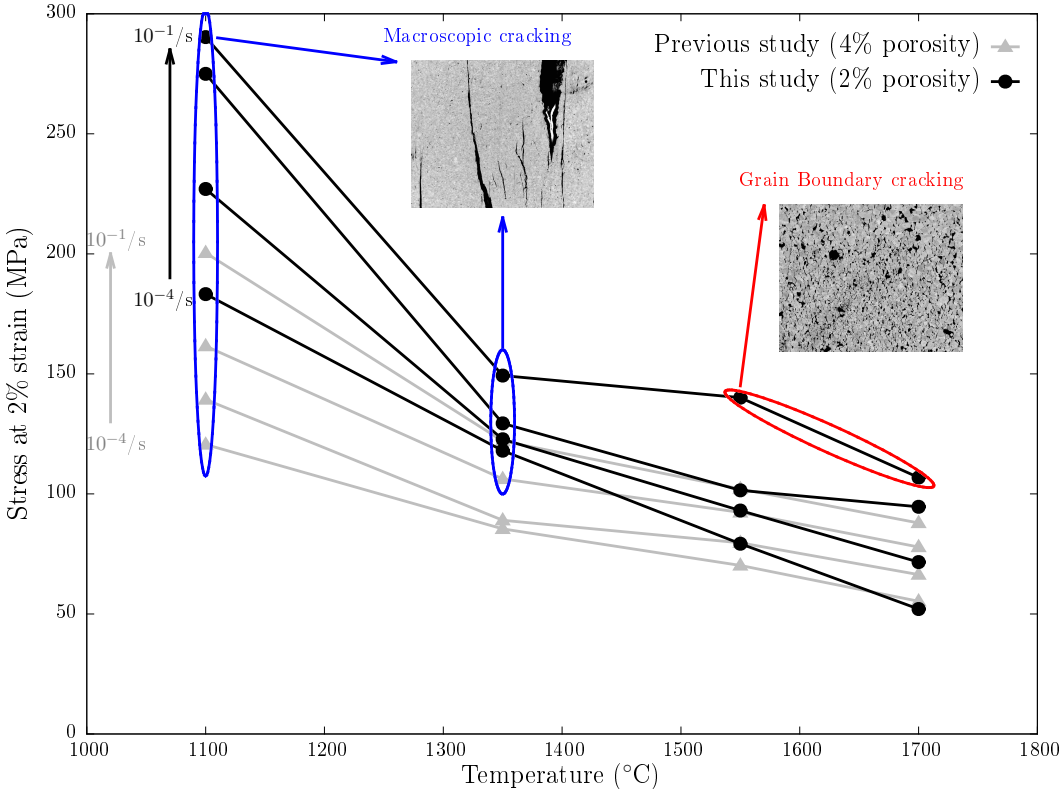

Figure 10: Synthesis of the test results in terms of stress at 2% strain versus temperature for all the strain rates, including data from a previous study on a UO_2 with a 4% initial porosity [26].

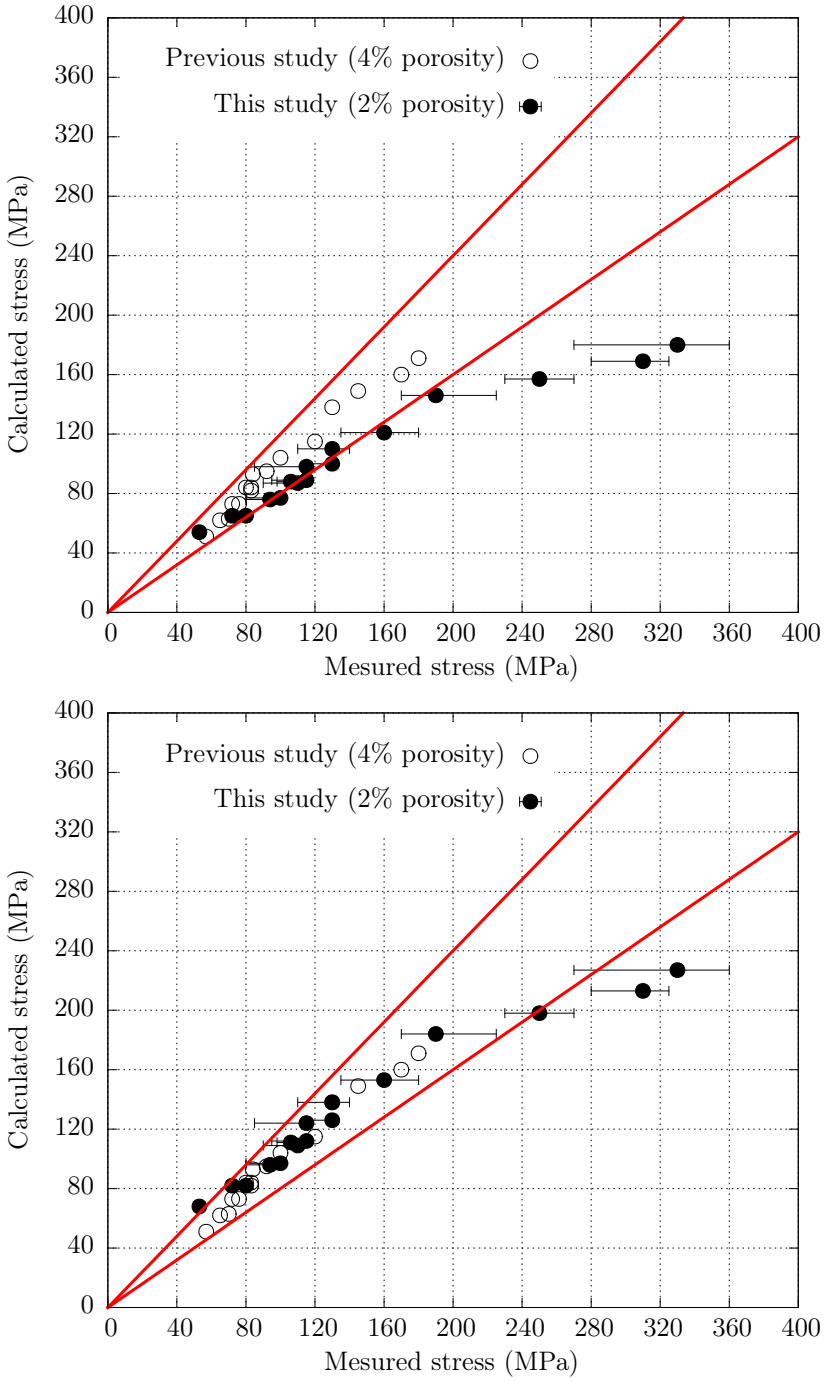

Figure 11: Calculated and measured compression stresses for two UO_2 with porosities 2% (this study) and 4% [26]. Top graph: $\sigma_0 = 5$ MPa for both materials. Bottom graph: $\sigma_0 = 6.3$ MPa for the 2% porosity UO_2, $\sigma_0 = 5$ MPa for the 4% porosity UO_2. The solid lines indicate the $\pm 10\%$ confidence interval. The horizontal bars give the stress peak magnitude.

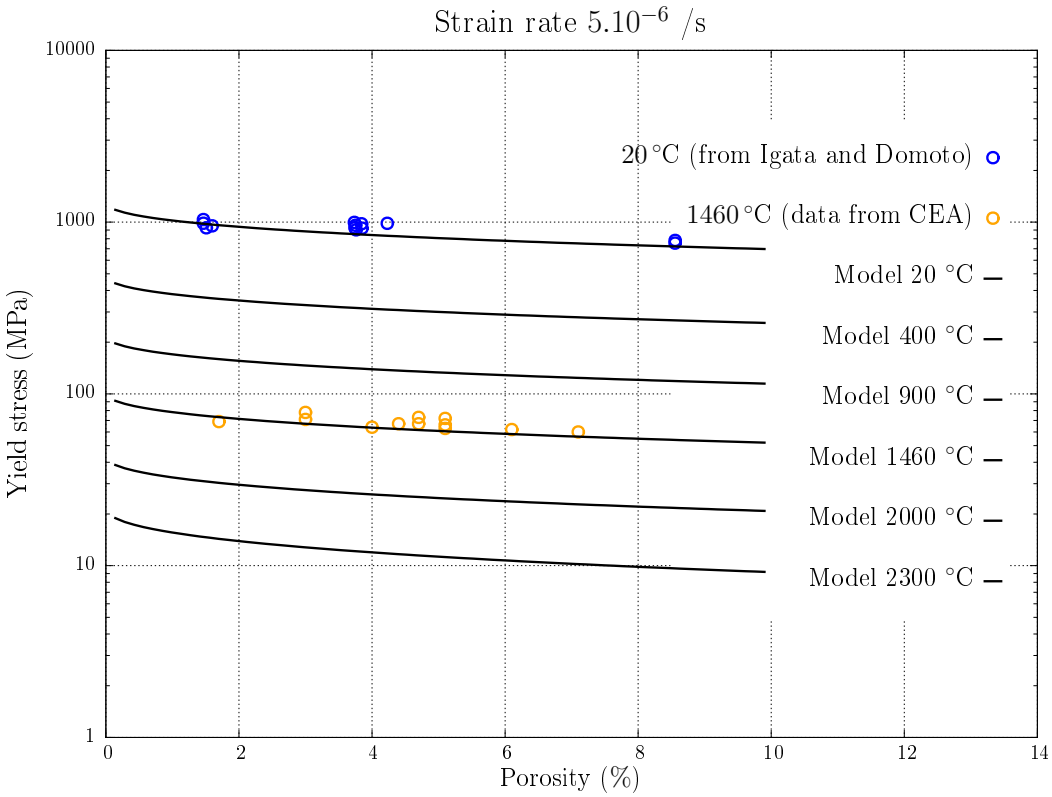

Figure 12: Evolution of the compressive yield stress of UO_2 with temperature and porosity (strain rate 5.10^{-6}/s). Comparison with room temperature measurements from Igata and Domoto [21] (porosity 2 to 9%, grain size ~ 10 μm, strain rate $\sim 10^{-6}$/s) and from an internal CEA study [35] (temperature 1450°C, porosity 1 to 8%, grain size $8-15$ μm, strain rate $\sim 10^{-5}$/s).

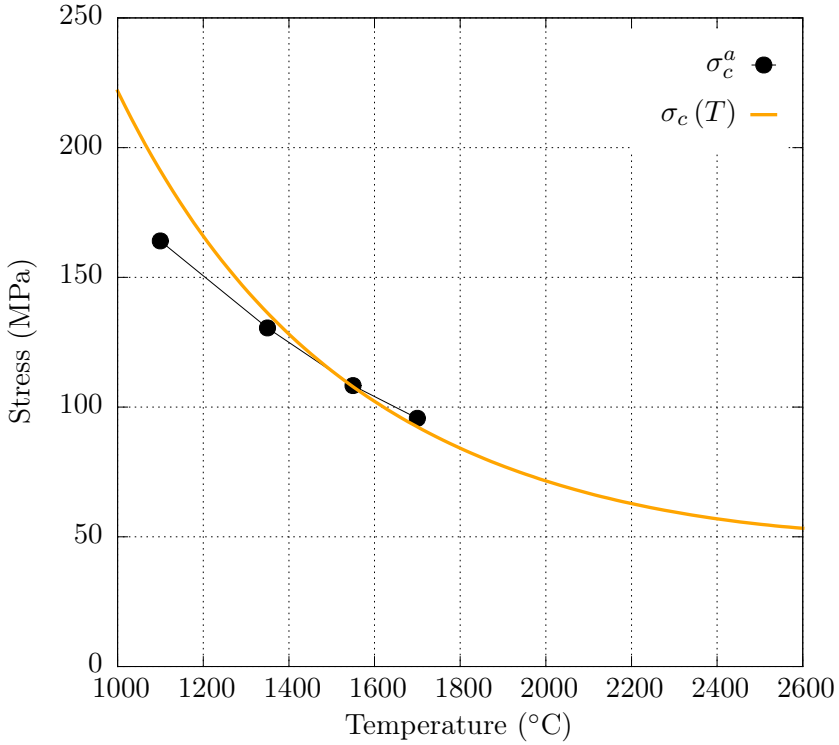

Figure 13: Evolution of the GB yield stress in compression in function of temperature. The maximum equivalent stresses $\sigma_c^a = \frac{1+\tau}{2\tau}(\sigma_{eq} + \omega\sigma_m)$ calculated in the FE simulations during the tests performed at 10^{-1}/s are also indicated.

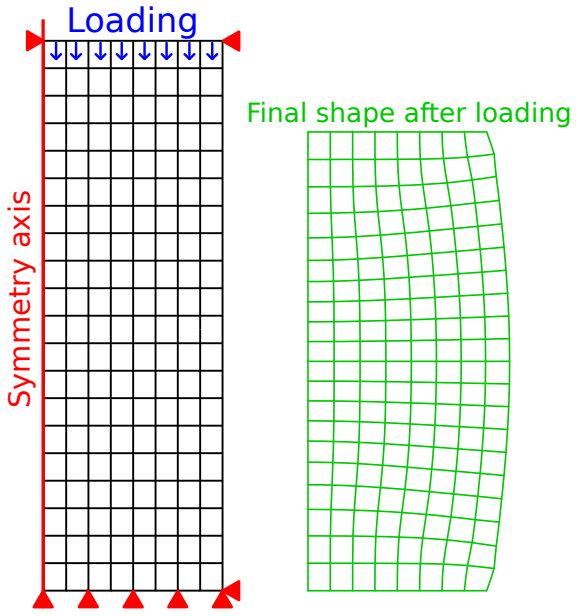

Figure 14: Mesh and boundary conditions in the simulations of the strain-driven compressive test.

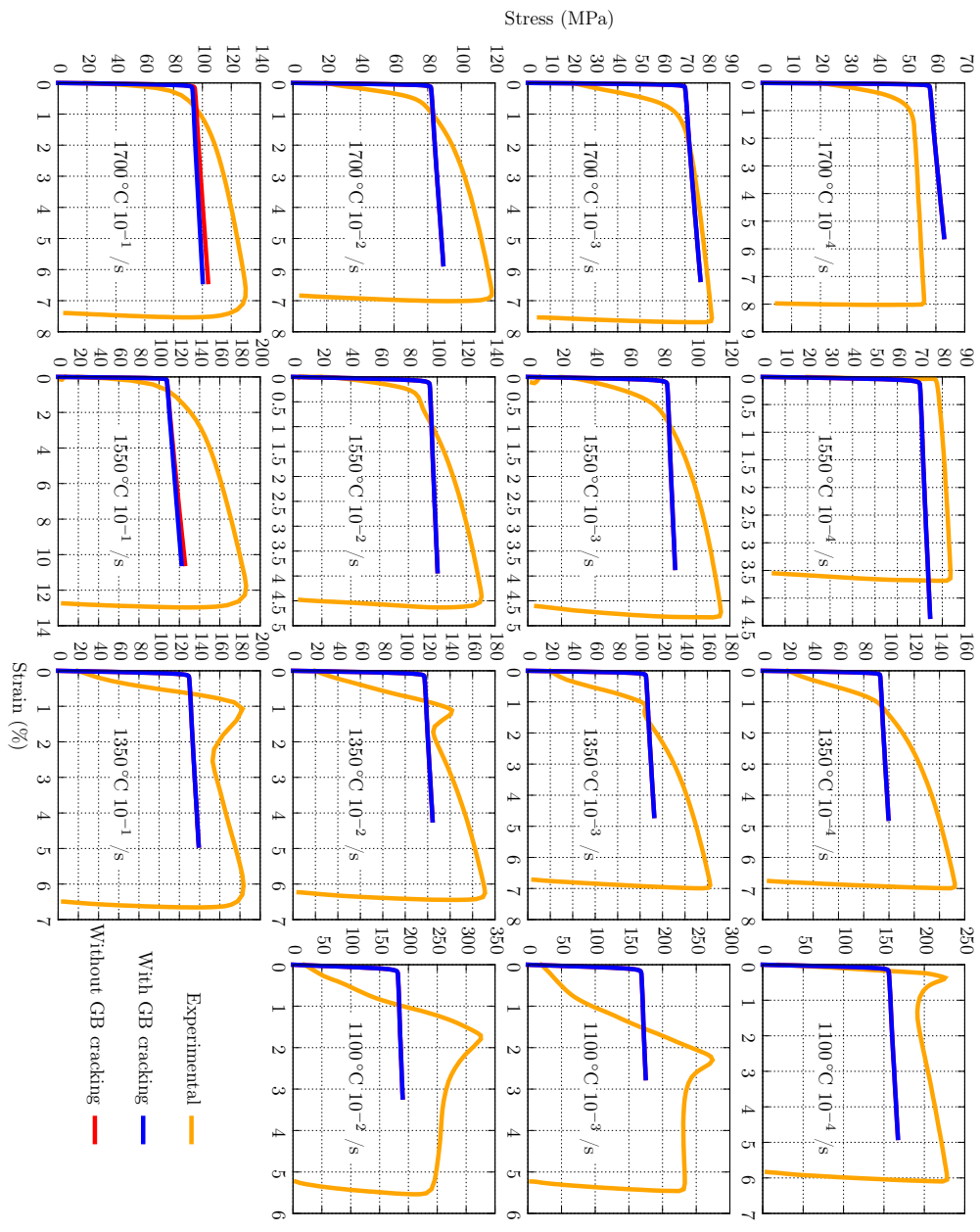

Figure 15: Calculated and measured stress-strain curves in all the tests.

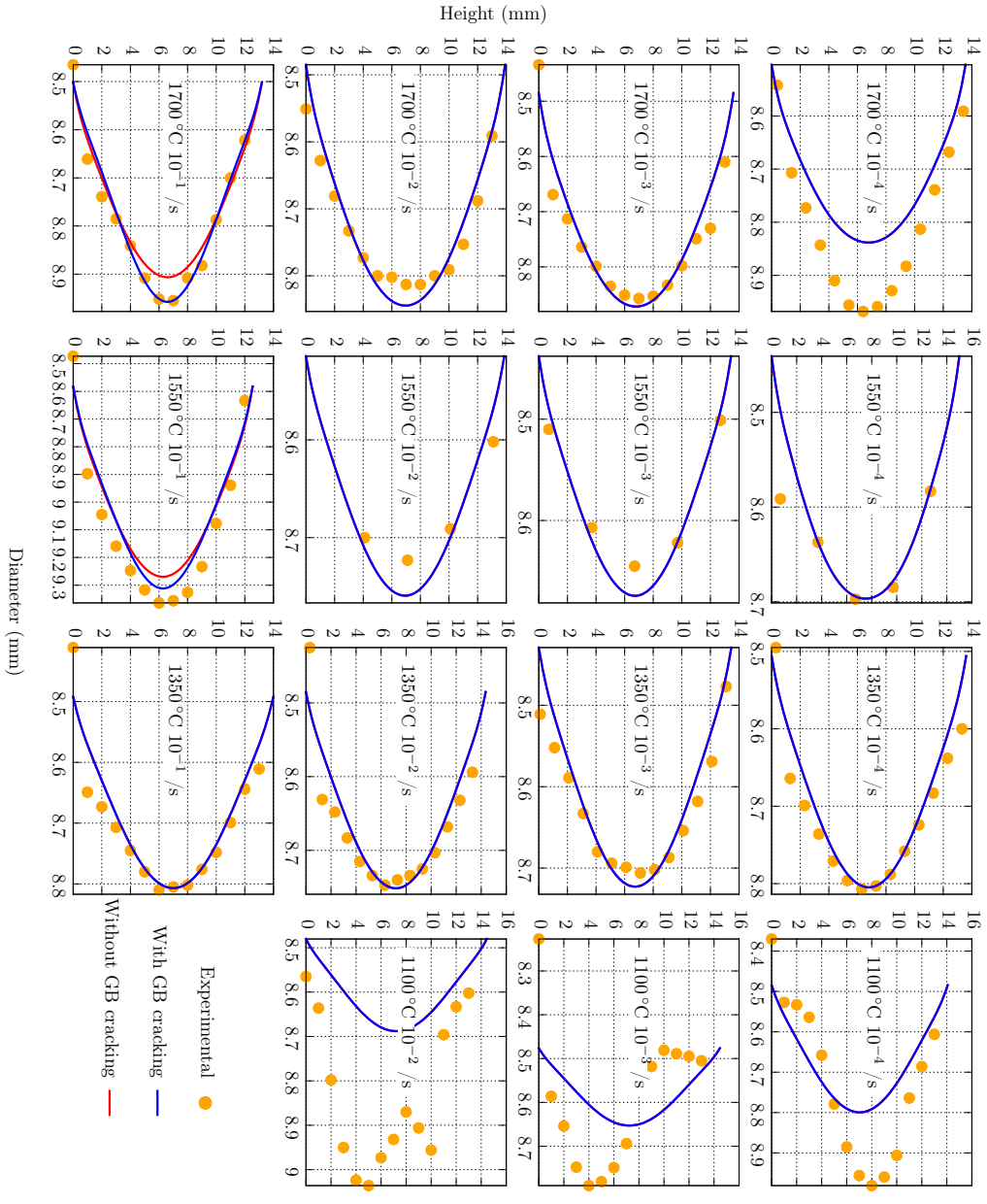

Figure 16: Calculated and measured diameter axial profiles after all the tests.

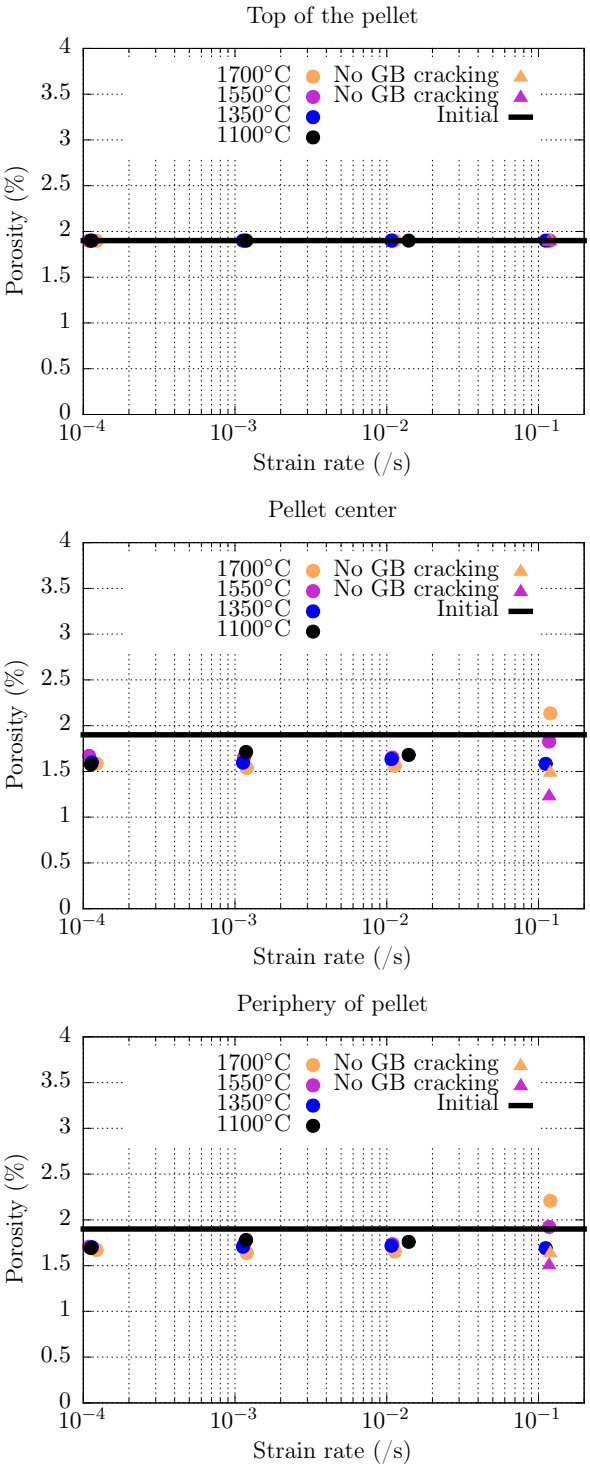

Figure 17: Calculated porosities at the top, center and periphery of the samples after all the tests.

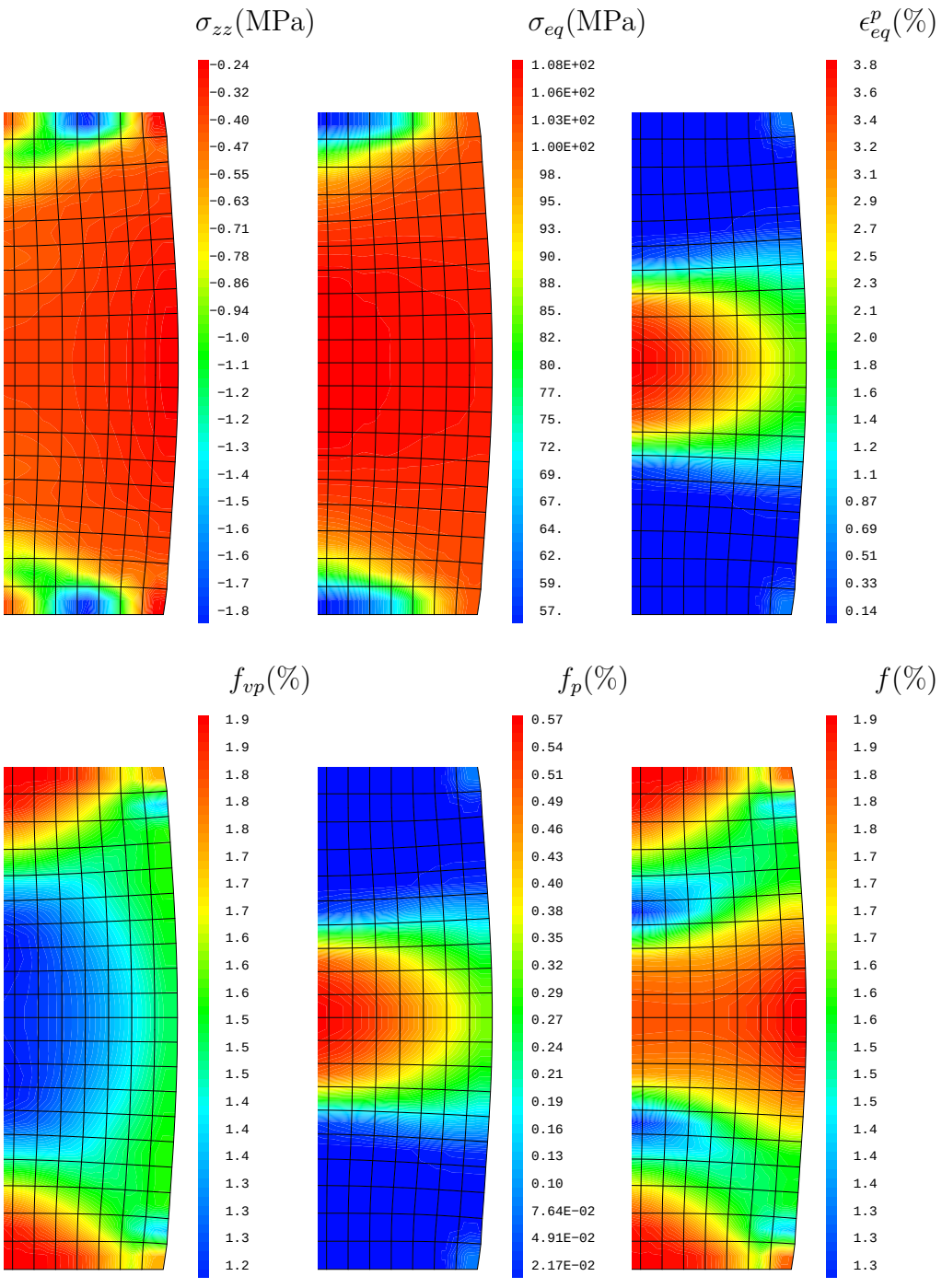

Figure 18: Isovalues of axial (σ_{zz}) and equivalent (σ_{eq}) stresses, equivalent plastic strain (ϵ^p_{eq}), viscoplastic porosity (f_{vp}, no GB cracking), plastic porosity (f_p), total porosity (f) during the test at 1550°C and 10^{-1}/s.

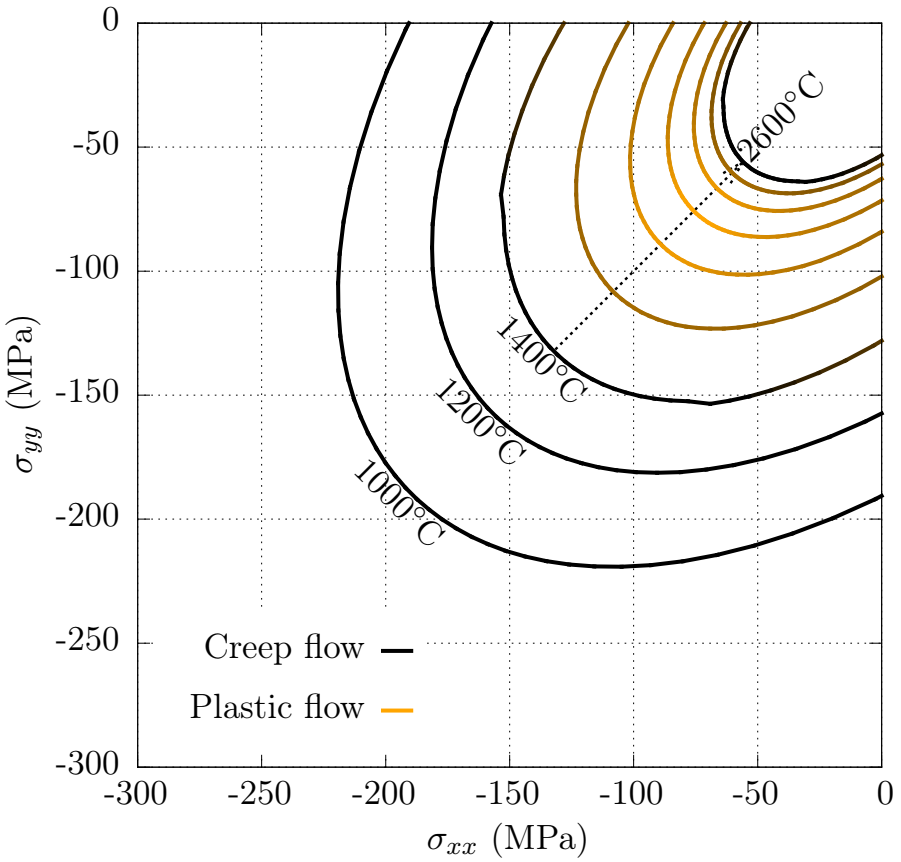

Figure 19: Biaxial yield surface obtained at an equivalent strain rate of 1/s showing the temperature and stress domains where plasticity (bright lines) or viscoplasticity (dark lines) control the material behaviour.

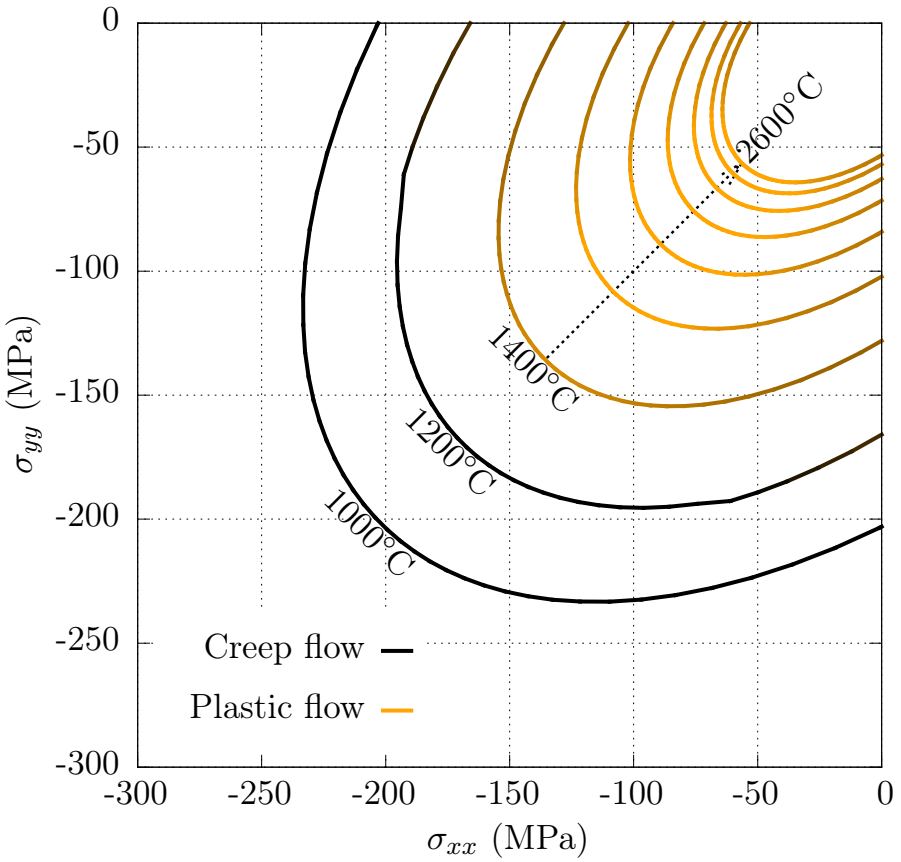

Figure 20: Biaxial yield surface obtained at an equivalent strain rate of 10/s showing the temperature and stress domains where plasticity (bright lines) or viscoplasticity (dark lines) control the material behaviour.